Environment-Robust Polarization-Based Phase-Shift Dynamic Demodulation Method for Optical Fiber Acoustic Sensor

Shuang Wang, Wenyan Liu, Junfeng Jiang, Zhiyuan Li, Peng Zhang, and Tiegen Liu

***Abstract*—In this paper, an environment-robust polarization-based phase-shift dynamic demodulation method for optical fiber acoustic sensor is proposed. Through optical lever effect of polarization low-coherence interference and amplitude scaling differential cross multiplication (AS-DCM) algorithm, acoustic-source induced interference phase of the acoustic sensor can be demodulated in real-time with high precision. The maximum relative phase demodulation error was only 0.694% when the cavity length had an offset ∼4 μm. The maximum cavity length demodulation error was keeping less than 3.988 nm under the optical power reduced ten times, which demonstrated an ultra-stable demodulation for the largest permitted optical power attenuation range, to our best knowledge. The proposed method has a capability of tolerating large optical power attenuation and large cavity length random offset, providing an environment-robust way for optical fiber acoustic sensor working in extreme environments.**

***Index Terms*—Fabry-Perot sensor, amplitude scaling differential cross multiplication, low-coherence interference, phase demodulation, signal compensation.**

I. Introduction

ACOUSTIC sensing has wide applications in wearable human physiological mechano-acoustic signal monitoring [1], [2], human-machine interaction in smart device voice user interface [3] or social robotics [4], ultrasound imaging [5], [6], and acoustic characteristics acquiring for aerospace [7]. Though electro-acoustic sensors still occupied the dominant position of acoustic-vibration detection, optical-acoustic sensors have acquired intensive attention in recent year due to their natural essence of electromagnetic interference immunity, high sensitivity and extreme environment resistance [8]–[10]. Among the optical-acoustic sensors, the extrinsic Fabry-Perot interferometric (EFPI) optical fiber acoustic sensors have simplest structure with compact size by modulating acoustic information into the cavity length [11]–[13]. It is worth to note that the acoustic sensing system performance is determined by both EFPI acoustic sensor and its demodulator [14]. The EFPI acoustic sensor may change the cavity length and reflecting optical power due to the effect of ambient environment [15]. Precisely discerning the tiny cavity length variation corresponding to acoustic source from environment disturbing is critical [16]. In addition, the demodulator itself may also expose to harsh environment [17]. Therefore, it is of far-reaching significance to establish an environment-robust demodulation method that can circumvent the problems from both the sensor and demodulator.

Direct interference intensity demodulation method has fast interrogation speed for acoustic sensing, however, its performance limited severely by unstable operating point of the EFPI sensor in the linear operating region [18], [19]. The differential cross multiplication (DCM) phase demodulation [20] method does not have the above limitation and provide a way for large-dynamic-range and wide bandwidth acoustic signal. Many configurations based on dual-wavelength or three-wavelength were proposed to realize the DCM phase demodulation. J. Xia *et al.* demonstrated a wavelength-switched phase interrogator with broadband source, polarization-maintaining fiber Bragg grating and electro-optic modulator (EOM) for EFPI sensors having different cavity lengths by using the ellipse fitting DCM algorithm [21]. However, the necessary stability control on EOM and high temperature-sensitivity fiber Bragg grating makes the system complex. H. Liao *et al.* realized DCM phase extraction with ASE broadband source and tunable filter to select two wavelengths for constructing quadrature signals [22], accompanying by the stability cost of low signal to noise ratio (SNR) resulting from little filtered optical power. In order to overcome the problem of low signal optical power, we used two narrowband tunable distributed feedback (DFB) laser diodes for specified cavity length [7]. J. Jia *et al.* showed a three-wavelength passive demodulation technique with three DFB laser diodes for arbitrary cavity length and it tolerated the bending loss of the leading fiber [23]. However, the above methods are inevitably affected by the wavelength random shift of the DFB sources or wavelength filters. Besides constructing phase step from the wavelength change, the phase step can also be realized from the optical path differences (OPD) change. In our previous research, we proposed orthogonal phase shift as well as four-step phase shift with birefringent crystals [24], [25]. Lacking the compensation consideration on real-time optical power attenuation prevents its application in dynamic extreme environment such as Mars-like planet exploration task.

Manuscript received October 9, 2021; revised November 10, 2021; accepted November 11, 2021. Date of publication November 16, 2021; date of current version December 14, 2021. This work was supported in part by the National Natural Science Foundation of China under Grants 62075160, 61735011, and 62035006. *(Corresponding authors: Junfeng Jiang; Tiegen Liu.)*

The authors are with the School of Precision Instrument and Optoelectronics Engineering, Tianjin University, Tianjin 300072, China (e-mail: shuangwang@tju.edu.cn; 525032917@qq.com; jiangjfjxu@tju.edu.cn; zhiyuanli@tju.edu.cn; zp90731@163.com; tgliu@tju.edu.cn).

Digital Object Identifier 10.1109/JPHOT.2021.3128447

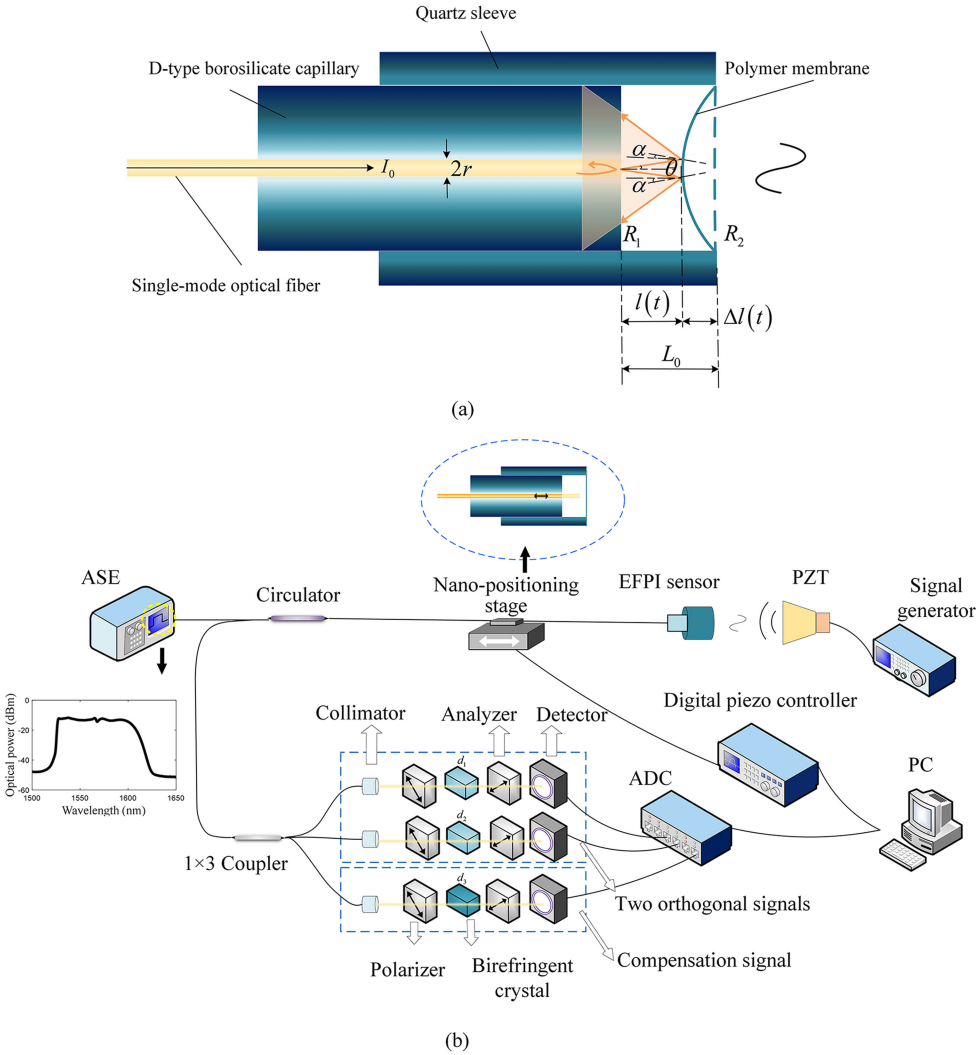

Fig. 1. (a) Schematic diagram of EFPI sensor structure, (b) schematic diagram of the environment-robust phase demodulation system.

In this paper, an environment-robust polarization-based phase-shift dynamic demodulation method for optical fiber acoustic sensor is proposed. With the help of optical lever effect of polarization low-coherence interference, three birefringent crystal blocks with selected thickness are used to construct two orthogonal low-coherence interference signals and a reference compensation DC component signal through OPD-based phase shifts. The extreme low temperature-insensitive property of birefringent crystal block and scale down effect ensure excellent thermal stability of phase shift steps. The acoustic-vibration induced interference phase change is then obtained with our proposed amplitude scaling DCM algorithm (AS-DCM). The experiment showed that the maximum relative phase demodulation error is only 0.694% when the cavity length has a large offset up to $\sim$4 μm. The cavity length maximum demodulation error can still be less than 3.988 nm for cavity length variation amplitude 1.943 μm and the optical signal power reduced 10 times, which is the largest permitted optical power attenuation range demonstrated among present phase-shift demodulation methods to our best knowledge. The proposed method can effectively reduce the affections caused by large cavity length random shift and large optical power attenuation, providing a robust solution for potential dynamic extreme environment application.

II. Operation Principle

Fig. 1(a) depicts the optical interference model of EFPI acoustic sensor. The acoustic sensor is composed of D-type borosilicate capillary, quartz sleeve, polymer membrane (polyphenylene sulfide, 1.2 μm thickness) and single-mode optical fiber (SMF), which are fixed by epoxy glue. D-type borosilicate capillary provides a micro air passage, and quartz sleeve plays the role of fixing and protection. The end face of SMF and the inner surface of the organic polymer membrane constitute a F-P microcavity. When the light enters the F-P microcavity, the light reflected by the end face and the light reflected by the diaphragm are coupled back to the optical fiber and interfere. The light intensity of the light beam returned through the first reflecting surface can be expressed as $I_{r1} = R_1 I_0 . R_1$ is the reflectivity of the SMF end face, $I_0$is the initial light intensity incident on the EFPI sensor. The light intensity of the beam coming back through the second

reflecting surface of diaphragm can be expressed as:

$$I_{r2}(t) = \left(1 - exp\left\{\frac{-2r^2}{[r + l(t)\tan\theta + l(t)\tan(\theta + 2\alpha)]^2}\right\}\right) \times (1 - R_1)^2 R_2 I_0. \quad (1)$$

where R_2 is the reflectivity of the inner surface of the diaphragm, r is the radius of the SMF core, θ is the divergence angle of the SMF and α is the angle of the curvature due to external acoustic vibration signal. t is time, $l(t)$is the working cavity length of the sensor, L_0 is the initial cavity length of the sensor and $\Delta L(t)$ is the change of cavity length caused by external dynamic acoustic signal. Under single wavelength, the interference intensity can be expressed as:

$$I_S(k,t) = I_{r1} + I_{r2}(t) + 2\sqrt{I_{r1}I_{r2}(t)}\cos[2kl(t)]. \quad (2)$$

where $k = 2\pi/\lambda$,λ is the wavelength.

The proposed AS-DCM algorithm adopts three-way low-coherence interference fringes to calculate. Fig. 1(b) shows the schematic diagram of the three-way phase demodulation system based on polarization interference technology. Nano-positioning stage realizes large cavity length variation of the EFPI sensor with digital piezo controller. The Broadband source (BBS) with Boxcar-like spectrum transmits light to EFPI sensor through a circulator. Reflected light is divided into three beams through a 1×3 coupler. Each beam passes through a polarizer, a small birefringent crystal block and an analyzer in sequence to form a low-coherent interference fringe, which is received by a detector. After analog-digital-converter (ADC) acquisition, the data is transmitted to the PC for processing.

The formed low-coherent interference fringe can be expressed as:

$$\begin{aligned} I_L(t) &= \int_{k_1}^{k_2} \rho G(k) I_S(k,t) I_D(k)\, dk \\ &= \frac{1}{2}\rho[I_{r1} + I_{r2}(t)]\left(\int_{k_1}^{k_2} G(k)dk \right. \\ &\quad - \int_{k_1}^{k_2} G(k)\cos(k\Delta nd)dk \\ &\quad + \beta(t)\int_{k_1}^{k_2} G(k)\cos[2kl(t)]\,dk \\ &\quad - \frac{\beta(t)}{2}\int_{k_1}^{k_2} G(k)\cos\{k[2l(t) + \Delta nd]\}\,dk \\ &\quad \left. - \frac{\beta(t)}{2}\int_{k_1}^{k_2} G(k)\cos\{k[2l(t) - \Delta nd]\}\,dk\right). \end{aligned} \quad (3)$$

where $G(k)$ is the BBS spectrum and $I_D(k)$ is the transfer function of demodulator interferometer.$\rho$is the optical power coefficient and equal to the ratio of the received actual optical power and the nominal optical power, which reflects the degree of optical power attenuation. Δn is the refractive index difference between extraordinary ray (E-ray) and ordinary ray(O-ray) of MgF_2birefringent crystal and d is the thickness of birefringent crystal. $k_i = 2\pi/\lambda_i, (i = 0, 1, 2)$.$\lambda_0$ is BBS center wavelength.λ_1, $\lambda_2$are the maximum and minimum wavelengths of the BBS, respectively. $\beta(t) = 2[I_{r1}I_{r2}(t)]^{\frac{1}{2}}/[I_{r1} + I_{r2}(t)]$. Because the magnitude of $l(t)$ is tens of microns and the tail swing of the negative first-order low-coherence interference fringes at the sensor cavity length can be ignored compared with the first-order low-coherence interference fringes, Formula (3) can be approximately simplified as following:

$$I_L(t) \approx A + B(t)\cos\{k_0[2l(t) - \Delta nd]\}. \quad (4)$$

Considering the box-like spectrum of ASE light source, the integrated low-coherent interference signal is similar to sinc function with sidelobe effect. In order to reduce the sidelobe effect, the cavity length of the EFPI sensor $L_0 = 90\ \mu$m. According to the principle of low coherent interference, the thicknesses of MgF_2birefringent crystal blocks are $d_1 = 2L_0/\Delta n = 15$ mm, and $d_2 = \lambda_0/4\Delta n + d_1 \approx 15.03$ mm. The third crystal block selected in the experiment is a-barium metaborate(a-BBO) birefringent crystal block with a thickness of 15 mm, and its birefringence index meets $\Delta n' = 10\Delta n$. The OPD introduced by the a-BBO crystal block is much greater than the length of low coherent interference, so the DC component of low coherent interference is obtained and removed in real-time. The center wavelength of BBS used in the experiment is 1566 nm and $d_2 - d_1 = 32.6\ \mu$m.The three-way output signals can be expressed as:

$$I_1(t) = A_1 + B_1(t)\cos\{k_0[2l(t) - \Delta nd_1]\}, \quad (5)$$

$$\begin{aligned} I_2(t) &= A_2 + B_2(t)\cos\{k_0[2l(t) - \Delta nd_2]\} \\ &= A_2 + B_2(t)\sin\{k_0[2l(t) - \Delta nd_1]\}, \end{aligned} \quad (6)$$

$$I_3 = A_3. \quad (7)$$

where A_1, A_2 are the DC components of two orthogonal low-coherence interference signals respectively, A_3 is the reference DC component signal. $B_1(t)$, $B_2(t)$ are the AC coefficients of two orthogonal low-coherence interference signals. Implement the following subtraction transformations:

$$I_4(t) = I_1(t) - I_3 = \Delta A_{13} + B_1(t)\cos\{k_0[2l(t) - \Delta nd_1]\}, \quad (8)$$

$$I_5(t) = I_2(t) - I_3 = \Delta A_{23} + B_2(t)\sin\{k_0[2l(t) - \Delta nd_1]\}. \quad (9)$$

The phase $\phi(t)$ of EFPI sensor can be expressed as:

$$\begin{aligned} \phi(t) &= \int \frac{I_4(t)I_5'(t) - I_5(t)I_4'(t)}{I_4^2(t) + I_5^2(t)}dt \\ &= \int \frac{2k_0 l'(t) I_4(t) \times B_2(t)\cos\{k_0[2l(t) - \Delta nd_1]\}}{I_4(t)^2 + I_5(t)^2}dt \\ &\quad + \int \frac{2k_0 l'(t) I_5(t) \times B_1(t)\sin\{k_0[2l(t) - \Delta nd_1]\}}{I_4(t)^2 + I_5(t)^2}dt. \end{aligned} \quad (10)$$

where $I_4'(t), I_5'(t)$ are the differentials of two orthogonal signals after removing the DC component. The thickness difference of the crystal block used to form two orthogonal signals is small enough so that $B_1(t) \simeq B_2(t) = B(t)$. When ΔA_{13} , ΔA_{23}

TABLE I
PARAMETERS OF SIMULATION

Symbol	Value	Description
λ_0	1566 nm	The center wavelength of BBS
$\Delta\lambda$	80 nm	The FWHM of the BBS
Δn	0.012	The refractive index difference between E-ray and O-ray of birefringent crystal
d_1	15 mm	The first thickness of birefringent crystal
d_2	15.0326 mm	The second thickness of birefringent crystal
L	90 μm	The initial cavity length of the EFPI sensor
θ	8°	The divergence angle of the SMF
ρ	[0,1]	The normalized optical power coefficient
R_1	0.04	The reflectivity of the end face of the SMF
R_2	0.04	The reflectivity of the inner surface of the IM
r	4.5 μm	The radius of the SMF core
λ_1	1526 nm	The minimum wavelengths of the BBS
λ_2	1606 nm	The maximum wavelengths of the BBS

satisfy the relation that $\Delta A_{i3}/A_i \leq 2\times10^{-3}, \Delta A_{i3}/B_i(t) \leq 1\times10^{-2}, (i=1,2)$, the phase demodulation error of AS-DCM is 2.371 nm when the peak to peak value (Vpp) of the acoustic signal to be measured is 2 μm. This demodulation error is within the allowable error range, so the information of EFPI sensor cavity length can be obtained by using the AS-DCM algorithm, which can be approximately expressed as:

$$\phi(t) = \int \frac{I_4(t)\, I_5'(t) - I_5(t)\, I_4'(t)}{I_4^2(t) + I_5^2(t)} dt \simeq 2k_0 l(t) + \mathrm{Z}. \tag{11}$$

where Z is a constant and is related to the initial phase. Through the above processing, the AC coefficients in the interference signals can be removed by reduction in real-time. The affections caused by the optical power fluctuation and the working cavity length shift because of thermal interference and mechanical vibration can be reduced.

III. SIMULATION

To illustrate the affections of cavity length shift and optical power attenuation on low-coherence interference intensity and phase demodulation result, we conduct the following simulation. The parameters are set as in Table I.

A. Cavity Length Shift Affection Simulation

The initial cavity length of the sensor L_0 is set to 90 μm and the acoustic-induced cavity length variation signal is set to $\Delta l(t) = 10^{-7}\cos(40\pi t)$. Fig. 2 shows low coherence interference waveform variations and AS-DCM phase demodulation results whenL_0 shifts from 90 μm to 92 μm. The red and blue signals on the left and right represent the low coherent interference signals under 90 μm and 92 μm with visible differences. The signal waveform changes with the change of the sensor cavity length, which is a function of time. The green signals represent AS-DCM phase demodulation results. When L_0 is 90 μm, the phase demodulation result is [-0.803 rad, 0.804 rad] and when L_0 is 92 μm, the phase demodulation result is [-0.789 rad, 0.794 rad]. By calculation, the demodulation phase difference is 0.024 rad and the corresponding cavity length is only 3.021 nm. According to the low coherence characteristic of broadband light source, the limiting relationship between light source wavelength and sensor cavity length can be eliminated, and the change of AC coefficient caused by cavity length drift can be eliminated by AS-DCM algorithm in real-time. It can be concluded that the proposed method can well resist the affection of cavity length shift.

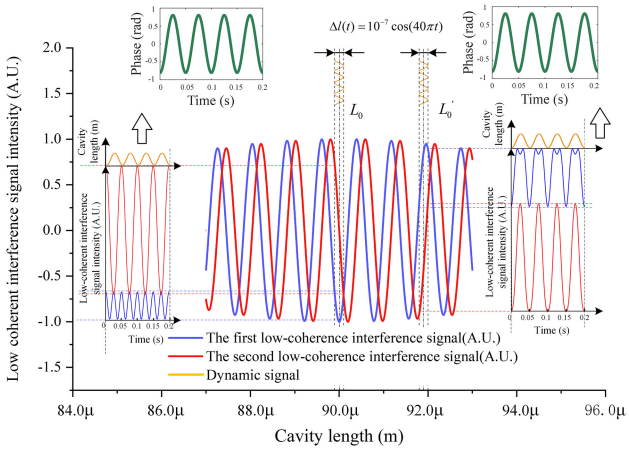

Fig. 2. Simulation of the affections of cavity length shift on low coherence interference and AS-DCM phase demodulation result.

B. Optical Power Attenuation Affection Simulation

Assuming the BBS has Boxcar-like spectrum profile attenuation, let the cavity length changes from 20 μm to 160 μm and the optical power coefficient to be 0.2, 0.4, 0.6, 0.8 and 1. The optical power coefficient of 1 means the actual optical power has no attenuation. The simulation result is shown in Fig. 3. It shows that attenuation of optical power can change the DC component and AC component amplitude of the low coherence interference signal. Set the frequency of the dynamic cavity length variation signal to 20 Hz and the amplitude to 1 μm. Normalize the two orthogonal signals under the situation that the optical power coefficient is 1. In this case, the demodulation result is considered to be the true value. The normalization coefficients are recorded to normalize when the optical power coefficient is 0.2, 0.4, 0.6 and 0.8. By using the traditional DCM [24] demodulation algorithm, which expression can

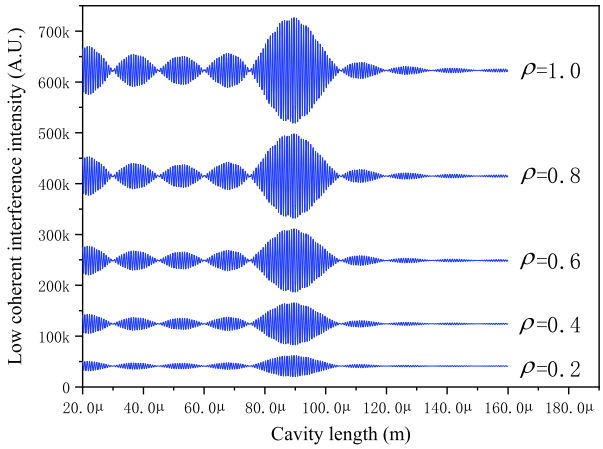

Fig. 3. Simulation of the affection of optical power attenuation on low coherence interference.

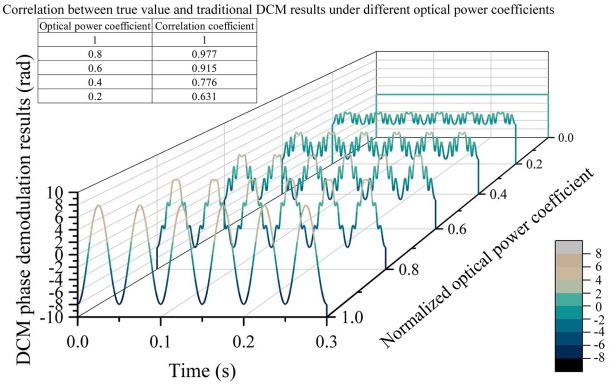

Fig. 4. Simulation of the affection of optical power attenuation on traditional DCM phase demodulation.

be expressed as:

$$\varphi(t) = \int (P_1 P_2{}' - P_1{}' P_2) dt. \tag{12}$$

where P_1, P_2 are two normalized sine and cosine signals, $P_1{}', P_2{}'$ are the differential functions of P_1, P_2. The demodulation results and their correlation under different optical power are shown in Fig. 4. When the optical power attenuates, the waveform demodulated by traditional DCM distorts. When optical power coefficient is 0.8, the correlation coefficient is 0.977, which means that the traditional DCM result losses the precise information of the acoustic signal. In view of the above shortcomings, we extract the DC component of the signal in real-time and propose AS-DCM to resist optical power attenuation affection. Fig. 5 shows the simulation of the affection of optical power attenuation on AS-DCM phase demodulation and the correlation between true value and AS-DCM results. It reveals that the correlation coefficients are always 1 when the optical power attenuates, which means AS-DCM has good resistance to optical power attenuation.

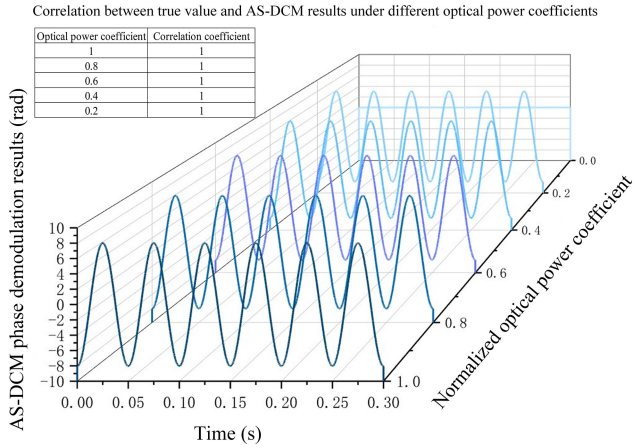

Fig. 5. Simulation of the affection of optical power attenuation on AS-DCM phase demodulation.

IV. Experiment and Discussion

A. Cavity Length Shift Affection Experiment

Though the end face of the SMF and the inner surface of the diaphragm constitute a parallel plate, the external acoustic signal can make the diaphragm bend. In addition, the temperature interference during demodulation leads to the thermal expansion of air medium and objects, resulting in a dynamic cavity length of the EFPI sensor. Both lead the cavity length to shift. To verify the affection of cavity length shift on phase demodulation, set the variable range of L_0 as [88.054 μm, 92.103 μm] with a step of 1 μm. Amplified spontaneous emission (ASE) source is selected as the broadband light source in the experiment and the output power is 50 mW. A single sine wave cavity length variation with frequency 20 Hz and amplitude 4.130 μm is generated by controlling the nano-positioning stage (P-622.1CD) to simulate acoustic vibration signal. When the output power of the light source is the maximum, the Vpp of the maximum noise voltage collected by ADC is 2.3 mV. Under the same birefringent crystal parameters, the optical power can be balanced at the computer program according to the three-way voltage ratio collected by ADC.

Fig. 6 shows the AS-DCM phase demodulation results, in which the red numbers indicate the peaks and valleys of the demodulated waveforms. Table II shows detailed analysis of this experiment. When L_0 changes from 88.054 μm to 92.103 μm, the minimum relative demodulation error is 0.182% and the maximum relative demodulation error is 0.694%. The main reason for the experimental error is that low coherence interference of ASE Box-like spectrum has sidelobe effect. The affection of the sidelobe is different under different cavity length, which introduces different degree of error to the demodulation results.

Ultrasonic source with frequency 22 kHz is then used to test proposed system. Set the variable range of L_0 as [88.302 μm, 92.201 μm] with a step of 1 μm. AS-DCM phase demodulation results and power spectral densities are shown as Fig. 7. The data analysis is shown as Table III. Using the average of five experiments as the reference value, the maximum

TABLE II
DATA ANALYSIS OF LOW-FREQUENCY DYNAMIC SIGNAL UNDER DIFFERENT INITIAL CAVITY LENGTH

Cavity length (μm)	AS-DCM demodulation phase value (rad)	Real phase value (rad)	Phase demodulation error (rad)	Cavity length demodulation error (nm)	Relative demodulation error (%)
88.054	33.027		0.113	14.082	0.341%
89.186	33.075		0.065	8.100	0.196%
90.205	33.370	33.140	-0.230	-28.662	0.694%
91.068	33.151		-0.011	-1.371	0.033%
92.103	33.272		-0.132	-16.450	0.398%

TABLE III
DATA ANALYSIS ULTRASONIC DYNAMIC SIGNAL UNDER DIFFERENT INITIAL CAVITY LENGTH

Cavity length (μm)	AS-DCM demodulation phase value (rad)	Average value (rad)	Phase demodulation error (rad)	Cavity length demodulation error (nm)
88.302	0.273		-0.002	-0.249
89.245	0.272		-0.001	-0.125
90.117	0.268	0.271	0.003	0.374
91.168	0.275		-0.004	-0.498
92.201	0.268		0.003	-0.374

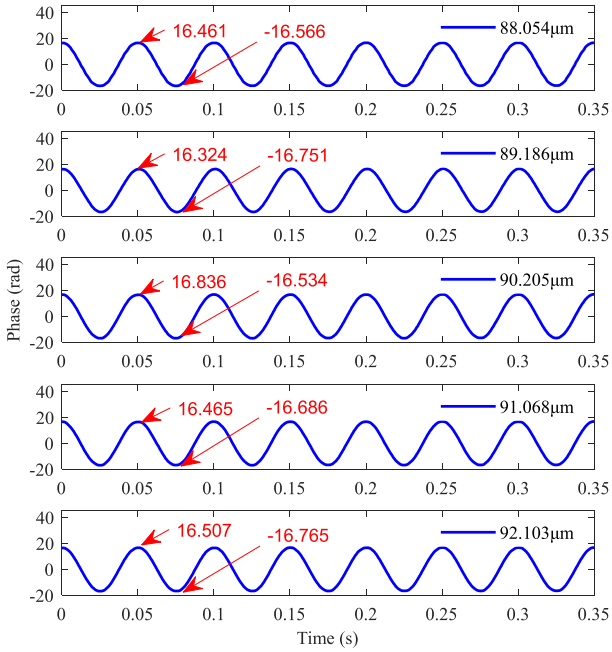

Fig. 6. AS-DCM phase demodulation results of low frequency dynamic signal under different initial cavity length.

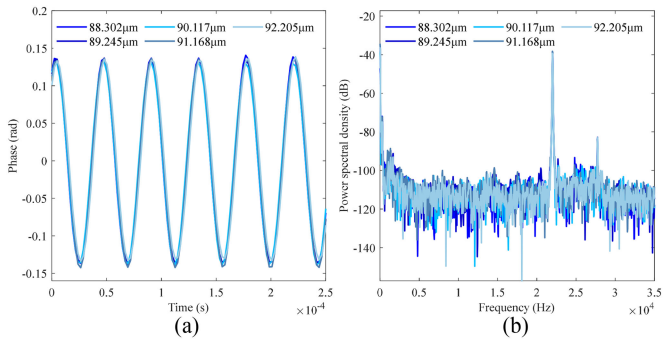

Fig. 7. AS-DCM phase demodulation results and power spectral densities of ultrasonic signal under different initial cavity length: (a) AS-DCM phase demodulation results, (b) power spectral densities.

cavity length demodulation error is 0.498 nm. The frequency demodulation accuracy is 0.082%, which verified the ability to demodulate high frequency acoustic vibration signal of the proposed method. Theoretically, this method has no upper limit of detection frequency. However, in practical application, the frequency demodulation range of acoustic vibration signal is physically limited by the response bandwidth of photodetector and the sampling frequency of ADC.

B. Optical Power Attenuation Experiment

To better demonstrate the advantage of the proposed method against optical power attenuation, a comparative experiment between AS-DCM and traditional DCM is carried out.

Set the initial optical power to 50 mW. In the demodulation process, adjust the optical power to 40 mW, 30 mW, 20 mW, 10 mW and 5 mW respectively to realize the attenuation of optical power. A single sine wave cavity length variation with frequency of 20 Hz and amplitude 1.943 μm is generated by controlling the nano-positioning stage to simulate acoustic vibration signal. Fig. 8 shows the Lissajous of dynamic signal under different ASE output power for AS-DCM and traditional DCM. It can be

TABLE IV
CORRELATION BETWEEN IDEAL VALUE AND LISSAJOUS FITTING CURVES UNDER DIFFERENT OUTPUT POWER UNDER AS-DCM

Output power of ASE (mW)	Fitting curve	Ideal curve	Correlation coefficient
50	$(x-0.0269)^2+(y-0.0522)^2=0.9621^2$	$x^2+y^2=1$	0.9911
40	$(x-0.0006)^2+(y-0.0195)^2=0.9617^2$		0.9942
30	$(x-0.0332)^2+(y-0.0076)^2=0.9775^2$		0.9920
20	$(x-0.0058)^2+(y-0.0259)^2=0.9500^2$		0.9923
10	$(x-0.0006)^2+(y-0.0195)^2=0.9617^2$		0.9907
5	$(x-0.0199)^2+(y-0.0468)^2=0.9109^2$		0.9748

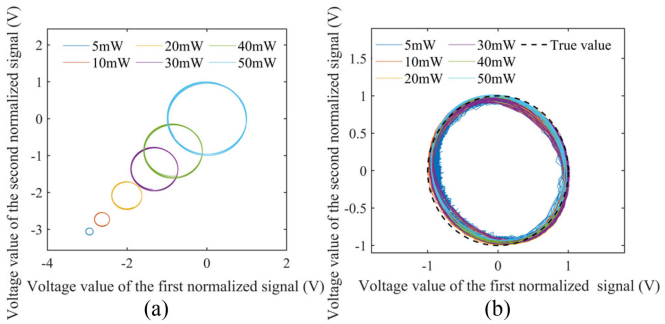

Fig. 8. Lissajous of dynamic signal with frequency of 20 Hz and amplitude of 1.943 μm under different ASE output power: (a) traditional DCM, (b) AS-DCM.

seen that the optical power attenuation sharply changes the DC components and AC coefficients of two orthogonal signals for traditional DCM. Lissajous is no longer approximate to the unit circle. After using the proposed method, the DC components and AC coefficients of the signals can be obtained in real-time and adjusted automatically. Fig. 8(b) provides the ideal unit circle and actual Lissajous of dynamic signal under different ASE output power for AS-DCM. Table IV shows the fitting results of the Lissajous in the Fig. 8(b) as well as the correlation between Lissajous actual fitting curves and ideal curve. It is worth to notice that when the output power of the ASE is more than 10 mW, the correlation coefficients between the Lissajous actual fitting curves and the ideal curve are not less than 0.9907. Continue to reduce the optical power to 5 mW, the correlation coefficient is can still keep 0.9748. That verified AS-DCM demodulation ensures the Lissajous still have good consistency under different optical power.

Fig. 9 shows the phase demodulation results of dynamic signal under different ASE output power between AS-DCM and traditional DCM. For traditional DCM, due to the optical power attenuation, the demodulation waveform is distorted, making the demodulation amplitude erroneous and resonance phenomenon occur. The experimental results in Fig. 9(a) are in good agreement with the simulation in Fig. 4. Fig. 9(b) shows AS-DCM phase demodulation results, in which the red numbers indicate the peaks and valleys of the demodulated waveforms. From Table V, the maximum cavity length demodulation error

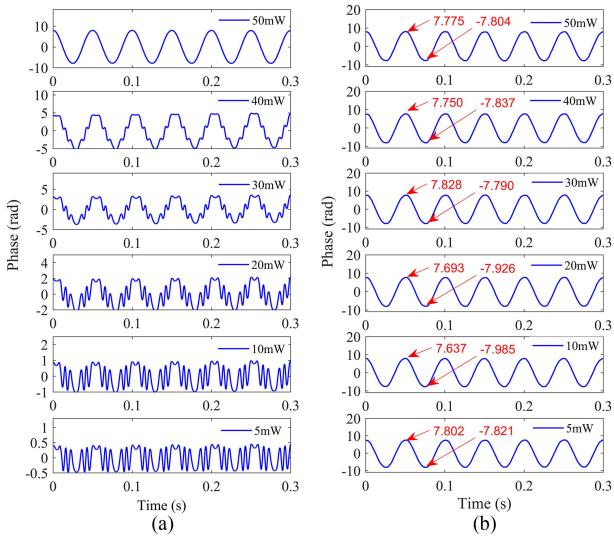

Fig. 9. Phase demodulation results of dynamic signal with frequency of 20 Hz and amplitude of 1.943 μm under different ASE output power before and after compensation: (a) traditional DCM, (b) AS-DCM.

calculated by AS-DCM demodulation technology is 3.988 nm when dynamic cavity length amplitude is 1.943 μm. The minimum relative demodulation error is 0.026% and the maximum relative demodulation error is only 0.205%, which verified the robustness of our proposed method under large optical power attenuation.

V. CONCLUSION

In this paper, an environment-robust polarization-based phase-shift dynamic demodulation method is proposed to detect acoustic vibration signal. We simulate the affections of initial cavity length shift and optical power attenuation on the phase demodulation results calculated by AS-DCM and traditional DCM, which are in good agreement with the experimental results. When the initial cavity length shifts from 88.054 μm to 92.103 μm, the maximum relative phase demodulation error is only 0.694%. The maximum cavity length demodulation error is less than 3.988 nm under the optical power reduced ten times, which demonstrates an ultra-stable demodulation for the largest permitted optical power attenuation range, to our best

TABLE V
DATA ANALYSIS OF OPTICAL POWER ATTENUATION EXPERIMENT UNDER AS-DCM

Output power of ASE (mW)	AS-DCM demodulation phase value (rad)	Real phase value (rad)	Phase demodulation error (rad)	Cavity length demodulation error (nm)	Relative demodulation error (%)
50	15.579	15.591	0.012	1.495	0.077%
40	15.587		0.004	0.498	0.026%
30	15.618		-0.027	-3.365	0.173%
20	15.619		-0.028	-3.489	0.180%
10	15.622		-0.031	-3.863	0.199%
5	15.623		-0.032	-3.988	0.205%

knowledge. The experimental results show that the proposed method can not only demodulate low-frequency dynamic signal but also demodulate ultrasonic signal with high precision. It can effectively reduce the affections caused by the optical power attenuation and the working cavity length shift with excellent stability and robustness, providing an ultrastable way for optical fiber acoustic sensor working in extreme environments.

Disclosures: The authors declare no conflicts of interest.

REFERENCES

[1] Y. Liu *et al.*, "Epidermal mechano-acoustic sensing electronics for cardiovascular diagnostics and human-machine interfaces," *Sci. Adv.*, vol. 2, no. 11, Nov. 2016, Art. no. e1601185, doi: 10.1126/sciadv.1601185.

[2] K. Lee *et al.*, "Mechano-acoustic sensing of physiological processes and body motions via a soft wireless device placed at the suprasternal notch," *Nature Biomed. Eng.*, vol. 4, no. 2, pp. 148–158, Nov. 2019, doi: 10.1038/s41551-019-0480-6.

[3] H. S. Wang *et al.*, "Biomimetic and flexible piezoelectric mobile acoustic sensors with multiresonant ultrathin structures for machine learning biometrics," *Sci. Adv.*, vol. 7, no. 7, Feb. 2021, Art. no. eabe5683, doi: 10.1126/sciadv.abe5683.

[4] H. Guo *et al.*, "A highly sensitive, self-powered triboelectric auditory sensor for social robotics and hearing aids," *Sci. Robot.*, vol. 3, no. 20, Jul. 2018, Art. no. eaat2516, doi: 10.1126/scirobotics.aat2516.

[5] W. J. Westerveld *et al.*, "Sensitive, small, broadband and scalable optomechanical ultrasound sensor in silicon photonics," *Nature Photon.*, vol. 15, no. 5, pp. 341–345, May 2021, doi: 10.1038/s41566-021-00776-0.

[6] A. Lakshmanan *et al.*, "Acoustic biosensors for ultrasound imaging of enzyme activity," *Nature Chem. Biol.*, vol. 16, no. 9, pp. 988–996, Jul. 2020, doi: 10.1038/s41589-020-0630-X.

[7] J. Jiang *et al.*, "Noncontact ultrasonic detection in low-pressure carbon dioxide medium using high sensitivity fiber-optic Fabry-Perot sensor system," *J. Lightw. Technol.*, vol. 35, no. 23, pp. 5079–5085, Dec. 2017, doi: 10.1109/JLT.2017.2765693.

[8] J. A. Guggenheim *et al.*, "Ultrasensitive plano-concave optical microresonators for ultrasound sensing," *Nature Photon.*, vol. 11, no. 11, pp. 714–719, Nov. 2017, doi: 10.1038/s41566-017-0027-x.

[9] A. M. Shrivastav, D. S. Gunawardena, Z. Liu, and H. Tam, "Microstructured optical fiber based Fabry-Perot interferometer as a humidity sensor utilizing chitosan polymeric matrix for breath monitoring," *Sci. Rep.*, vol. 10, no. 1, Apr. 2020, Art. no. 6002, doi: 10.1038/s41598-020-62887-y.

[10] Y. Wang *et al.*, "A comprehensive study of optical fiber acoustic sensing," *IEEE. Access.*, vol. 7, pp. 85821–85837, Jun. 2019, doi: 10.1109/ACCESS.2019.2924736.

[11] Y. Liu, D. N. Wang, and W. P. Chen, "Crescent shaped Fabry-Perot fiber cavity for ultra-sensitive strain measurement," *Sci. Rep.*, vol. 6, Dec. 2016, Art. no. 38390, doi: 10.1038/srep38390

[12] W. P. Chen, D. N. Wang, B. Xu, C. L. Zhao, and H. F. Chen, "Multimode fiber tip Fabry-Perot cavity for highly sensitive pressure measurement," *Sci. Rep.*, vol. 7, no. 1, Mar. 2017, Art. no. 368, doi: 10.1038/s41598-017-00300-x.

[13] S. Wang and W. Chen, "A large-area and nanoscale graphene oxide diaphragm-based extrinsic fiber-optic Fabry-Perot acoustic sensor applied for partial discharge detection in air," *Nanomaterials,* vol. 10, no. 11, Nov. 2020, Art. no. 2312, doi: 10.3390/nano10112312.

[14] C. Zhang, H. Zhu, and B. Shi, "Role of the interface between distributed fibre optic strain sensor and soil in ground deformation measurement," *Sci. Rep.*, vol. 6, Nov. 2016, Art. no. 36469, doi: 10.1038/srep36469.

[15] Y. Liu, B. Qi, and D. E. Winder, "Faraday Michelson interferometers for signal demodulation of fiber-optic sensors," *J. Lightw. Technol.*, vol. 39, no. 8, pp. 2552–2558, Apr. 2021, doi: 10.1109/JLT.2021.3053370.

[16] J. Zhang, W. Rui, C. Ma, Y. Cheng, X. Liu, and J. Christensen, "Remote whispering metamaterial for non-radiative transceiving of ultra-weak sound," *Nature Commun.*, vol. 12, Jun. 2021, Art. no. 3670, doi: 10.1038/S41467-021-23991-3.

[17] G. Lu *et al.*, "High-temperature-resistant silicon-polymer hybrid modulator operating at up to 200 Gbit s^{-1} for energy-efficient datacentres and harsh-environment applications," *Nature Commun.*, vol. 11, no. 1, Aug. 2020, Art. no. 4224, doi: 10.1038/s41467-020-18908-5.

[18] F. Wang, J. Xie, Z. Hu, S. Xiong, H. Luo, and Y. Hu, "Interrogation of extrinsic Fabry-Perot sensors using path-matched differential interferometry and phase generated carrier technique," *J. Lightw. Technol.*, vol. 33, no. 12, pp. 2392–2397, Jun. 2015, doi: 10.1109/JLT.2014.2379943.

[19] Q. Liu *et al.*, "Quadrature phase-stabilized three-wavelength interrogation of a fiber-optic Fabry-Perot acoustic sensor," *Opt. Lett.*, vol. 44, no. 22, pp. 5402–5405, Nov. 2019, doi: 10.1364/OL.44.005402.

[20] S. Zhang, A. Zhang, and H. Pan, "Eliminating light intensity disturbance with reference compensation in interferometers," *IEEE Photon. Technol. Lett.*, vol. 27, no. 17, pp. 1888–1891, Sep. 2015, doi: 10.1109/LPT.2015.2444421.

[21] J. Xia, S. Xiong, F. Wang, and H. Luo, "Wavelength-switched phase interrogator for extrinsic Fabry-Perot interferometric sensors," *Opt. Lett.*, vol. 41, no. 13, pp. 3082–3085, Jul. 2016, doi: 10.1364/OL.41.003082.

[22] H. Liao, P. Lu, L. Liu, D. Liu, and J. Zhang, "Phase demodulation of fabry-perot interferometer-based acoustic sensor utilizing tunable filter with two quadrature wavelengths," *Proc. SPIE Photonic Instrum. Eng. IV*, Feb. 2017, Art. no. 101101J, doi: 10.1117/12.2251749.

[23] J. Jia, Y. Jiang, H. Gao, L. Zhang, and Y. Jiang, "Three-wavelength passive demodulation technique for the interrogation of EFPI sensors with arbitrary cavity length," *Opt. Exp.*, vol. 27, no. 6, pp. 8890–8899, Mar. 2019, doi: 10.1364/OE.27.008890.

[24] Y. Huang *et al.*, "Orthogonal phase demodulation of optical fiber fabry-perot interferometer based on birefringent crystals and polarization technology," *IEEE Photon. J.*, vol. 12, no. 3, Jun. 2020, Art. no. 7101209, doi: 10.1109/JPHOT.2020.2977952.

[25] J. Jiang *et al.*, "Optical fiber fabry-perot interferometer based on phase-shifting technique and birefringence crystals," *Opt. Exp.*, vol. 26, no. 17, pp. 21606–21614, Aug. 2018, doi: 10.1364/OE.26.021606.